3-D Multistatic Ground Penetrating Radar Imaging for Augmented Reality Visualization

Mauricio Pereira, Dylan Burns, Daniel Orfeo, Yu Zhang[®], Liangbao Jiao, Dryver Huston, and Tian Xia[®], Senior Member, IEEE

Abstract—Ground penetrating radar (GPR) is a useful instrument for smarter infrastructure applications, in particular, for the localization and mapping of underground infrastructure and other subsurface assets, due to its ability to sense metallic and nonmetallic buried objects. For instance, air-coupled, multistatic GPR could potentially be employed to quickly produce subsurface maps for public and private stakeholders, enabling rational and more efficient planning of underground infrastructure inspection, maintenance, and construction. An application of interest in such context is a faster identification of underground utilities location and depth by innovative data visualization methods, such as augmented reality. A 3-D model of the subsurface asset is desirable for such applications. However, raw GPR data is often hard to interpret. Imaging algorithms are applied to improve GPR data readability and signal-to-noise ratio by focusing the spread energy. Here, a processing pipeline that takes raw 3-D multistatic GPR data as input and yields a 3-D model as output is proposed. Initially, a 3-D back-projection algorithm is applied to air-coupled, multistatic GPR data to recover buried target localization. An enhancement filter, tailored for tubular structures, is applied to reduce background noise and highlight structures of interest in the 3-D image. This process is successfully applied to three laboratory scenarios of plastic buried targets with different sizes and shapes.

Index Terms—3-D feature extraction, augmented reality (AR), back-projection algorithm (BPA), enhancement filter, ground penetrating radar (GPR), imaging, multistatic radar, smart infrastructure, synthetic aperture radar.

I. INTRODUCTION

ROUND penetrating radar (GPR) is a remote geophysical sensing method based on the scattering of elec-

Manuscript received July 7, 2019; revised October 31, 2019; accepted December 20, 2019. Date of publication February 6, 2020; date of current version July 22, 2020. This work was supported by NSF Grant No. 1647095 and No. 1640687, the University of Vermont (UVM) SparkVT Fund and Vermont Established Program to Stimulate Competitive Research (EPSCoR) program. (Corresponding author: Tian Xia.)

Mauricio Pereira was with the Department of Mechanical Engineering, The University of Vermont, Burlington, VT 05405 USA. He is now with Princeton University, Princeton, NJ 08544 USA.

Dylan Burns, Daniel Orfeo, and Dryver Huston are with the Department of Mechanical Engineering, The University of Vermont, Burlington, VT 05405 USA.

Yu Zhang is with the Department of Electronics and Safety, Delphi Automotive, Agoura Hills, CA 91301 USA.

Liangbao Jiao is with the Department of Telecommunications and Engineering, Nanjing Institute of Technology, Nanjing 211167, China.

Tian Xia is with the Department of Electrical and Biomedical Engineering, The University of Vermont, Burlington, VT 05405 USA (e-mail: txia@uvm.edu).

Color versions of one or more of the figures in this article are available online at http://ieeexplore.ieee.org.

Digital Object Identifier 10.1109/TGRS.2020.2968208

tromagnetic (EM) waves [1], [2]. It has been applied in the detection of geological features [3], [4], inspection of bridge decks and railroad ballast [5], [6], detection of concrete rebar [7], self-driving vehicles [8], and localization and assessment of buried utilities [9]. This last application makes GPR a good tool for smart infrastructure applications, as underground assets are often aging in unknown location and condition. Current commercial GPR systems are commonly ground-coupled, however, for faster surveys, air-coupled GPR systems are desired. Multistatic GPR systems can reduce survey time even more by covering a larger area, or yet provide a more comprehensive assessment of the subsurface. A high-speed GPR could inspect a bridge deck without blocking traffic, reducing survey costs [10].

Furthermore, advances in smartphone sensor suites and computing power have enabled the potential of mobile augmented reality (AR) applications in smart infrastructure [11], [12]. A desirable feature is to visualize underground assets in AR to facilitate post-survey localization of buried utilities. The GPR data could be used in AR visualization of the subsurface, but raw GPR data is generally hard to interpret, as point scatterers emerge as hyperbolas in 2-D GPR scans or as hyperboloids in 3-D GPR scans. To improve data readability and increase signal-to-noise ratio (SNR), migration or imaging algorithms are used to focus the acquired backscattered waves, with potential recovery of the scattering target surface shape. Imaging algorithms may be further leveraged to produce 3-D models of underground utilities that could be used in AR applications to indicate their position. Ozdemir et al. [13] studied several migration methods, such as Stolt migraton [14], Kirchhoff migration [15], and so on, and assessed in terms of focusing performance and computation time. The study reveals that one of the most promising imaging algorithms is the time-domain back-projection algorithm (BPA). The advantages of the BPA include its suitability for parallel computing, capability of integrating data collected in arbitrary survey trajectories, and natural formulation for layered structures, such as air-ground. In multistatic GPR systems, the data acquired by different receivers may not be simply stacked or averaged, as these receivers have different time delays due to their spatial offsets. The BPA can properly account for the antenna's spatial offset and project distinct receiver images to the actual spatial coordinates. This is in contrast with frequency-domain imaging algorithms that require regular grid samples for

0196-2892 © 2020 IEEE. Personal use is permitted, but republication/redistribution requires IEEE permission. See https://www.ieee.org/publications/rights/index.html for more information.

efficient fast Fourier transform (FFT), frequency domain interpolation, and phase compensations to fuse each receiver image [16], [17].

Heading toward an automated, real-time survey and AR visualization, a processing methodology that yields a 3-D representation of important features present in the imaged subsurface is of interest. The challenges in this task are manifold. For instance, in a multistatic radar system, each antenna may vary in specifications, leading to different SNRs among different antennas. In addition, due to the antenna's spatial offset, each antenna covers a different area or footprint. If a buried target is sensed only by one receiver, formation of multistatic images by simple superposition of subsurface images from each receiver may obfuscate the available information and cause image distortion, jeopardizing the advantage of multistatic GPR, or making the detection of low-intensity targets in the image difficult.

The presence of important signals at different intensity levels in the same image is a difficulty that also exists in medical imaging. For instance, extraction of 3-D models of the vascular system is challenging due to the different intensities present in the image. Those differential intensities may be due to various diameters of the vascular structure, nonuniformity of the contrast bolus distribution within the vascular network. and complex branch structure [18]-[20]. To circumvent this issue, several enhancement filters have been proposed in the vascular imaging literature to ease segmentation of 3-D angiograms [21]. Owing to the tubular and spherical nature of vascular elements, a large class of enhancement filters are developed based on the Hessian of the 3-D image which conveys local information about the shape of a structure within the image [20]. Such class of enhancement filters may be applicable in GPR imaging of tubular and spheroid targets, such as utility pipes and landmines, respectively, to enhance features and facilitate extraction of a 3-D model from the image.

The novel contribution of this article is to propose a data-processing scheme that takes as input multistatic ground or air-coupled GPR data and outputs a 3-D model of relevant features of the image by combining a 3-D multistatic BPA with a Hessian-based enhancement filter, in pursuit of AR visualization of buried utilities. To the best of the authors' knowledge, this is the first processing pipeline combining a BPA with an enhancement filter toward smart infrastructure applications.

This article is organized as follows: In Section II, the BPA for ground and air-coupled GPR system for both the 2-D and 3-D cases is introduced. The initial part of the algorithm has been presented in [22], but here a different approach is proposed for the fusion of each receive—antenna pair image. In Section III, an overview of the processing pipeline is given and a Hessian-based enhancement filter is presented. In Section IV, results for three laboratory experiments are presented and discussed. The concluding remarks are given in Section V.

II. BACK-PROJECTION ALGORITHM

In the BPA, the trace acquired by the GPR system at a scan position is back-projected into the space domain based on the wave travel time [16]. Performing this process for multiple

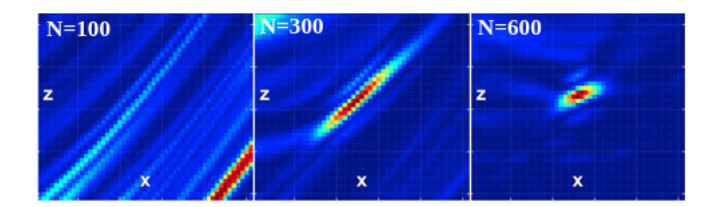


Fig. 1. As the number N of back-projected traces increases, the target is better focused. (a) Projection along the z-axis. (b) Projection along the x-axis. (c) Projection along the y-axis.

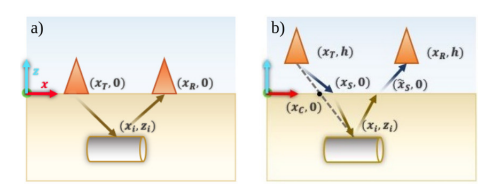


Fig. 2. Imaging scheme for 2-D (a) ground-coupled and (b) air-coupled GPRs.

GPR scan positions leads to the constructive superposition of the back-projected signals, enabling the recovery of the scattering object's position and/or shape. This target reconstruction process is illustrated in Fig. 1. The figure shows side view projection of the multistatic image. High-intensity values of each trace corresponding to the buried target are back-projected into the same subsurface region. As the number *N* of back-projected traces increases, the image target gets into focus, resolving its position and shape.

A fundamental step of the BPA is the accurate estimation of the wave travel time to the scattering point of interest in the domain. In Sections II-A and II-B, the wave travel time computation for several scenarios is presented. Assuming that receivers acquire the signal from each transmitter independently, the prototypic case for the multistatic formulation is the bistatic formulation. Hence, the wave travel times are initially computed for the bistatic radar.

A. Ground-Coupled GPR Scan

1) Two dimensions: Consider the imaging scheme for a ground-coupled bistatic GPR shown in Fig. 2(a). Let d_{AB} denote the Euclidean distance between two points A, B. Let P_i , with i = 1, ..., N, be a subsurface domain point, and P_T , P_R be the transmit and receive antenna positions, respectively. The total wave travel time from the transmitter to the point P_i and back to the receiver is given by

$$t(P_i, P_{\rm T}, P_{\rm R}) = \frac{d_{P_{\rm T}}P_i + d_{P_i}P_{\rm R}}{n}$$
(1)

where $v = c/\sqrt{\epsilon}$ is the wave speed, c is the speed of light in vacuum, and ϵ is the ground dielectric constant.

2) Three dimensions: In the ground-coupled GPR scan, extension to the 3-D scenario, illustrated in Fig. 3(a), is straightforward, requiring only the introduction of a third coordinate in the distance calculations.

B. Air-Coupled GPR Scan

1) Two dimensions: Consider the imaging scheme for an air-coupled bistatic GPR shown in Fig. 2(b). The total wave

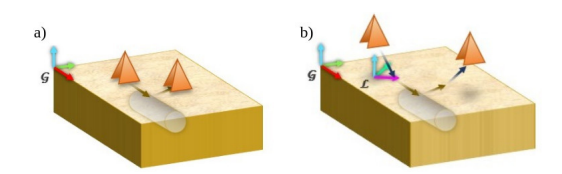


Fig. 3. Imaging scheme for 3-D (a) ground-coupled and (b) air-coupled GPRs.

travel time is given by

$$t(P_i, P_{\rm T}, P_{\rm R}) = \frac{d_{P_{\rm T}P_{\rm S}}}{c} + \frac{d_{P_{\rm S}P_i}}{v} + \frac{d_{P_i\tilde{P}_{\rm S}}}{v} + \frac{d_{\tilde{P}_{\rm S}P_{\rm R}}}{c}$$
(2)

where P_S and \tilde{P}_S are the interface scattering points. The point P_S is approximated as [23]:

$$x_{S}(P_{i}, P_{T}) = \begin{cases} x_{i} + \frac{x_{C} - x_{i}}{\sqrt{\epsilon}}, & \text{if } |x_{T} - x_{i}| < d_{cr} \\ x_{i} - \frac{z_{i}}{\sqrt{\epsilon - 1}}, & \text{if } x_{T} \ge x_{i} + d_{cr} \\ x_{i} + \frac{z_{i}}{\sqrt{\epsilon - 1}}, & \text{if } x_{T} \le x_{i} - d_{cr} \end{cases}$$
(3)

for $i=1,\ldots,N$, where x_C is the intersection point of a straight line connecting P_i to P_T and the air–ground interface. The same formula can be applied to determine the scattering point \tilde{P}_S on the signal return path by using the receiver position P_R in place of the transmitter position P_T . The distance criterion is given by $d_{cr}=(h-z_i)(\epsilon/\epsilon-1)^{1/2}$, where h is the antenna height above the ground level. Notice that the z-axis points upward, so the subsurface points P_i have negative z_i , such that d_{cr} is always positive. Here, it is assumed that the transmit and receive antennas stay at the same and constant height.

2) Three dimensions: For the 3-D case, illustrated in Fig. 3(b), (2) can also be applied by adding an extra spatial coordinate. The scattering points are then calculated by extending the approximation given in (3) through an homogeneous transformation between a global coordinate system $\mathcal G$ and a local coordinate system $\mathcal L$ whose x-axis is aligned with the antennas plane, depicted in Fig. 3(b), as explained in [22]. It yields the approximation

$$x_{S} = \begin{cases} x_{i} - \frac{z_{i}(x_{T} - x_{i})}{\sqrt{\epsilon}(h - z_{i})}, & \text{if } |x_{i} - x_{T}| \leq |\cos(\psi)|d_{cr} \\ x_{i} + \frac{z_{i}\cos(\psi)}{\sqrt{\epsilon - 1}}, & \text{if } |x_{i} - x_{T}| > |\cos(\psi)|d_{cr} \end{cases}$$
(4)

for i = 1, ..., N, with $y_S = y_T + ((y_i - y_T)/(x_i - x_T))(x_S - x_T)$, and $\cos(\psi) = (x_i - x_T/((x_i - x_T)^2 + (y_i - y_T)^2)^{1/2})$.

The same set of formulas can be applied using the receiver position P_R in place of P_T to calculate the scattering point position from the point P_i to the receiver antenna.

C. BPA Image Formation

In the image formation process, the wave travel times to all domain points P_i , $i=1,\ldots,N$, are computed for each $k=1,\ldots,M$ GPR scan position. Let $t_{i,k}=t(P_i,P_{\mathrm{T}}^k,P_{\mathrm{R}}^k)$ denote the total travel time to point P_i when the GPR system is at the kth position.

1) Bistatic: Let $s^k(t)$ be the signal acquired by the receiver at the kth position. The bistatic BPA image is formed as

$$\mathcal{I}(P_j) = \sum_{i=1}^{N} \sum_{k=1}^{M} s^k(t_{i,k}) \delta(P_i - P_j)$$
 (5)

where $\delta(\cdot)$ is the Kronecker delta.

Since there is an interest only in the image contrast, the image is scaled as $\mathcal{I}'(P_j) = (\mathcal{I}(P_j)/\mathcal{I}^{\max})$, where $\mathcal{I}^{\max} = \max |\mathcal{I}(P_i)|$.

2) Antenna Pattern: Let $g(\theta_{i,k})$ represent the antenna gain as a function of $\theta_{i,k}$, $i=1,\ldots,N$, the angle formed between the vertical axis and a line connecting the receiver to the ith domain point when the system is at its kth position. The bistatic image may be constructed accounting for the antenna radiation pattern by substituting $s^k(t_{i,k})$ in (5) by

$$s^{k}(\theta_{i,k}, t_{i,k}) = g(\theta_{i,k}) s_{0}^{k}(t_{i,k})$$
 (6)

where $s_0^k(t)$ denotes the trace acquired by the receiver at the kth position.

3) Multistatic: Consider a multistatic GPR system composed of Q transmitters and R receivers. Under the condition that the receivers acquire the signal from each transmitter independently, that is, $s_{q,r}^k(t)$, the signal acquired by the rth receiver from the qth transmitter at the kth position is available, the bistatic image $\mathcal{I}_{q,r}$ may be formed for each (q,r) transmitter–receiver pair, with $q=1,\ldots,Q, r=1,\ldots,R$, using (5), as

$$\mathcal{I}_{q,r}(P_j) = \sum_{i=1}^{N} \sum_{k=1}^{M} s_{q,r}^k(t_{i,k}) \delta(P_i - P_j)$$
 (7)

and scaled as $\mathcal{I}'_{q,r}(P_j) = (\mathcal{I}_{q,r}(P_j)/\mathcal{I}^{\max}_{q,r})$, where $\mathcal{I}^{\max}_{q,r} = \max_{1 \leq i \leq n} |\mathcal{I}_{q,r}(P_i)|$. Pereira et al. [22] formed the multistatic image by sum-

Pereira $e\bar{t}$ al. [22] formed the multistatic image by summing over all transmitter–receiver pairs images. Here, before summation, an intermediary image $\tilde{\mathcal{I}}_{q,r}$ is formed by squaring each voxel (l, m, n) of the bistatic image $\mathcal{I}_{q,r}$ as

$$(\tilde{\mathcal{I}}_{q,r}(P_j))_{l,m,n} = (\mathcal{I}_{q,r}(P_j))_{l,m,n}^2.$$
 (8)

Notice that the image is squared after back-projection, which is different from squaring the GPR data and back-projecting. Squaring the image casts it into a form proportional to power instead of voltage, lowering the noise level by weighing each signal proportionally to its amplitude.

The squaring of the image could have been performed after the summation of the initial $\mathcal{I}_{q,r}$ bistatic images but it is advantageous to perform it before summation due to the different footprints of each receive antenna. Each transmitter–receiver BPA image is well focused within its coverage area, but contains a significant amount of artifacts outside that coverage area. Artifacts from one receive antenna would introduce undesired signals in other receive antenna footprint region. For instance, consider the diagram shown in Fig. 4. The first receiver R_1 observes a subsurface region highlighted in blue. The antenna view is limited by its radiation pattern, but the back-projection process may not account for this effect accurately, especially in air-coupled scenarios. Because of

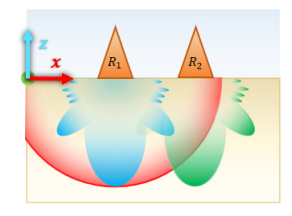


Fig. 4. First receiver, R_1 , back-projection region extends beyond (red) the antenna coverage region (blue). This causes artifacts to be introduced in the second antenna, R_2 , coverage region (green).

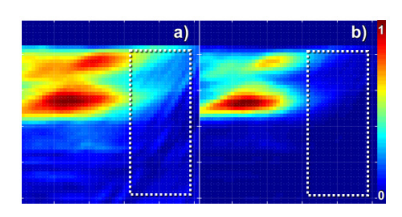


Fig. 5. Side-view projection illustrating the artifacts present in the area beyond a receive antenna footprint in (a) original bistatic image and the mitigation of these artifacts in (b) squared bistatic image.

this, the receiver R_1 back-projected signals extend beyond its field of view. This not observed area is shown in red, corresponding to an artifact region that is outside of antenna coverage. The artifact region is overlapped with the region covered by the second receiver R_2 , highlighted in green, which may result in distortion when all receivers' subsurface images are summed directly to form the multistatic image. Signals projected beyond the antenna's area of coverage have lower absolute values compared to the coverage area. Hence, squaring the signal before summation helps mitigate the artifacts because lower values will be penalized with smaller weights, whereas regions of high focus will be less penalized. Examples of these artifacts from one of the cases studied in this article (first receiver image of Case 1) are highlighted in Fig. 5(a), which shows a side-view projection of a normalized bistatic GPR image using the absolute values of the image data. The absolute values of the image were taken to prevent artificial attenuation of the projection by destructive interference along the projection axis since the original 3-D image has positive and negative artifacts. For comparison, the mitigation provided by squaring the image is evidenced in Fig. 5(b).

Squaring the original BPA images has the caveat of eliminating information concerning the relative values of the ground and the buried target's dielectric constant. For the target, for example, metallic object, whose dielectric constant value is higher than that of the ground, the backscattered signal has an opposite polarity from the incident signal, whereas for the target, for example, polymeric object, whose dielectric constant value is lower than that of the ground, the backscattered and the incident signals maintain the same polarity. Hence, one may infer the target material based on the phase shift of the scattered wave. Squaring the signal leads to lose of the signal phase polarity information and does not allow distinguishing these two cases. As a solution,

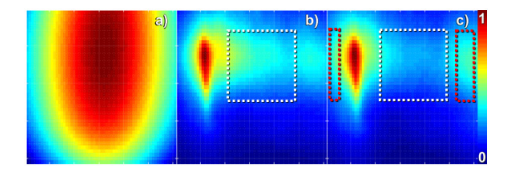


Fig. 6. Top-view projection illustrating (a) uneven distribution of the BPA. (b) Artificial highlighting of the BPA image. (c) Compensation by averaging, which reduces the effect on high-contribution areas but highlight low-contribution noisier regions.

if there is an interest in determining the buried target material, instead of only squaring the signal, one may preserve the signals of the original image, that is, define the voxel (l, m, n) of a second intermediary image as $(\mathcal{I}_{q,r}^{\pm}(P_j))_{l,m,n} = \text{sign}((\mathcal{I}_{q,r}(P_j))_{l,m,n})(\tilde{\mathcal{I}}_{q,r}(P_j))_{l,m,n}$, with $\tilde{\mathcal{I}}_{q,r}(P_j)$ as in (8), and $\text{sign}(\cdot)$ is the pixelwise sign function.

Here, the main interest is in imaging a subsurface target and extracting a representative 3-D model for AR visualization and not determining the target material. Hence, the multistatic image is formed using the squared values as

$$\mathcal{I}(P_j) = \sum_{q=1}^{Q} \sum_{r=1}^{R} \tilde{\mathcal{I}}_{q,r}(P_j). \tag{9}$$

III. IMAGE ENHANCEMENT AND MODEL EXTRACTION

Pereira et al. [22] used isosurfaces of manually selected values to obtain a representative 3-D model of the buried targets. This is possible in a low-noise image with a single simply shaped target whose dielectric constant is significantly different from the background. However, in more challenging cases, the image may have considerable background noise caused by many factors, for instance, by the different antenna specifications of the multistatic GPR system, presence of targets with dielectric constants closer to the ground rendering a small contrast between the background and the target, complex shape target, and so on. On top of this, the BPA introduces an artificial bias in the formed image associated with each antenna footprint. This bias can be visualized by back-projecting a constant unity signal in the domain. This process leads to Fig. 6(a), showing the top-view projection of the BPA signal contributions of a receive antenna in a multistatic GPR. Fig. 6(b) shows the artificial highlighting of the BPA image on the central-upper region where no buried targets are present due to this bias. Compensation of this effect could be implemented by, for example, averaging image voxel intensity over the number of signal contributions. It should be noted that the areas of high-density signal contributions are expected to exhibit better focusing and higher SNR as more signals are contributing to the image reconstruction. While compensating this bias works well in areas of high contribution, it leads to a higher weight of noisier regions of the image as shown in Fig. 6(c). Due to this duality, compensation of the BPA bias with such an approach might not be beneficial in general.

These characteristics of the BPA image together with the challenges associated with a multistatic radar system, such

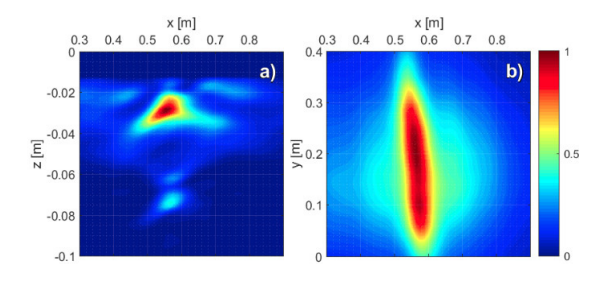


Fig. 7. Case 2: (a) Side-view projection illustrating the signal focusing at the top and bottom of a pipe cross section. (b) Top-view projection showing the tube-like structure of those regions.

as antenna performance variations, and different antenna orientations and associated polarization, calls for an enhancement process to facilitate image interpretation and 3-D model extraction.

As stated in Section I, the application interest of this article is detecting underground utilities that are usually of tubular forms, that is, the BPA image exhibits tube-like shapes, as depicted in Fig. 7. A Hessian-based enhancement filter, described in the section ahead, is applied on the BPA image to highlight tubular targets in the image, aiding in the 3-D model extraction process.

A. Hessian-Based Enhancement Filtering

Subsurface imaging presents challenges that bear similarity to vasculature imaging. For instance, the vascular network is immersed in a volume filled with other tissue structures, while in GPR imaging, the structures of interest, such as pipelines, are surrounded by a medium containing rocks, roots, soil layers, and so on. This causes the reconstructed structures of interest to be embedded in a noisy volume. Important elements of the vascular network, such as vessels, aneurysms, and bifurcations, have different dimensions and shapes, and respond differently to contrast bolus, rendering image analysis and processing difficult due to the different intensity values of those elements. The same may happen in GPR imaging if, for instance, the imaged region has targets of different materials, or if the geometry favors scattering in some directions depending on the antenna polarization, or if there are local changes on the ground, for example, different volumetric water content. In multistatic GPR, another challenge is to preserve the information collected by all receivers, since they observe different areas. Over-observed areas, that is, areas covered by more than one receive antenna, may saturate the multistatic image and hinder the preservation and visibility of low-intensity but important structures in the individual receiver images. Moreover, the geometry of the targets of interest in both vascular imaging and in the GPR application of interest here are tubular.

To address such issues, the vascular imaging community introduced several enhancement filters [19], [20], [24]–[26]. A class of such enhancement filters are based on the image derivatives, in particular, on the eigenvalues of the Hessian of the image which contain information regarding the shape of the imaged structure [19].

In Hessian-based methods, the image $\mathcal{I}(\mathbf{x}), x \in \mathbb{R}^D$ is expanded as

$$\mathcal{I}(\mathbf{x}_0 + \delta \mathbf{x}_{0,\sigma}) \approx \mathcal{I}_{0,\sigma} + \delta \mathbf{x}_0^T \nabla \mathcal{I}_{0,\sigma} + \frac{1}{2} \delta \mathbf{x}_0^T \mathcal{H}_{0,\sigma} \delta \mathbf{x}_0. \quad (10)$$

The symbol σ corresponds to the scale associated with a D-dimensional Gaussian distribution $G(\mathbf{x}, \sigma) =$ $(1/(2\pi\sigma^2)^{D/2})e^{(\|\mathbf{x}^T\mathbf{x}\|/2\sigma^2)}$, used to compute the derivatives by convolution as $(\partial/\partial x)\mathcal{I}(\mathbf{x},\sigma) = \sigma^{\gamma}\mathcal{I}(\mathbf{x}) * (\partial/\partial x)G(\mathbf{x},\sigma)$. The parameter γ defines a family of functions. As explained in [19], the second-order derivative of the Gaussian is able to identify contrasts in a scale σ . Thus, σ is a scale that can be chosen prior to segmentation based on GPR system parameters, for example, at the order of the wavelength of significant power transmitted, or determined offline through calibration. Eigenvalues and eigenvectors of the Hessian have an intuitive geometrical interpretation [19], [20] and convey information regarding the local image curvature. This implies that the Hessian eigenvalues can be used to identify tubular or spherical structures. Thus, such enhancement filters may be used to improve the BPA images of tubular structures, such as pipelines.

Enhancement filters are defined as functions $\nu: \mathbb{R}^D \to \mathbb{R}$ of the Hessian eigenvalues that amplify structures of interest in the image. Here, the Jerman enhancement filter (JEF) is chosen due to its superior efficacy in amplifying tubular structures [20]. Let $\mathcal{H} \in \mathbb{R}^{3\times3}$ be the Hessian of $\mathcal{I}(P)$ with $P \in \mathbb{R}^3$. Its eigenvalues are $\lambda_1, \lambda_2, \lambda_3$ with $|\lambda_1| \leq |\lambda_2| \leq |\lambda_3|$. The JEF is defined as

$$\nu(\lambda_{1}, \lambda_{2}, \lambda_{3}) = \begin{cases} 0, & \text{if } \lambda_{2} \leq 0 \lor \lambda_{\rho} \leq 0\\ 1, & \text{if } \lambda_{2} \geq \lambda_{\rho}/2 \geq 0\\ \lambda_{2}^{2}(\lambda_{\rho} - \lambda_{2}) \left[\frac{3}{\lambda_{2} + \lambda_{\rho}}\right]^{3}, & \text{otherwise} \end{cases}$$
(11)

where λ_{ρ} is the regularized λ_3 calculated as

$$\lambda_{\rho}(\lambda_{3}, \lambda_{\tau}) = \begin{cases} \lambda_{3}, & \text{if } \lambda_{3} > \lambda_{\tau} \\ \lambda_{\tau}, & \text{if } 0 < \lambda_{3} \leq \lambda_{\tau} \\ 0, & \text{otherwise} \end{cases}$$
 (12)

where $\lambda_{\tau} = \tau \max_{P} \lambda_{3}(P, \sigma)$, and $\tau \in [0, 1]$ is a filter parameter setting the filter maximum gain cutoff threshold. Higher τ values lead to higher λ_{ρ} values, meaning that less voxels of the image receive the maximum filter enhancement $(\nu = 1)$, since it is harder to satisfy the condition $\lambda_{2} \geq \lambda_{\rho}/2$. For instance, for $\tau = 1$, one has $\lambda_{\rho} = \max_{P} \lambda_{3}(P, \sigma)$, hence the maximum filter gain is applied only when λ_{2} is at least half of the maximum λ_{3} in the entire image. Conversely, lower values of τ makes the filter more sensitive, since more regions of the image will receive maximum enhancement. Further, in the JEF, $\gamma = 2$, that is, the Hessian components are proportional to the square of the scaling factor σ . Let $\mathcal{H}_{\mathcal{I}}(P_{j}): \mathbb{R}^{3} \to \mathbb{R}^{3}$ be a function returning the eigenvalues of the Hessian of the image \mathcal{I} at the point P_{j} . The enhanced image is obtained as $\mathscr{E}(P_{j}) = \nu(\mathcal{H}_{\mathcal{I}}(P_{j}))$.

Fig. 8 shows the top- and side-view projections of the original images (left column) and the Jerman filter-enhanced

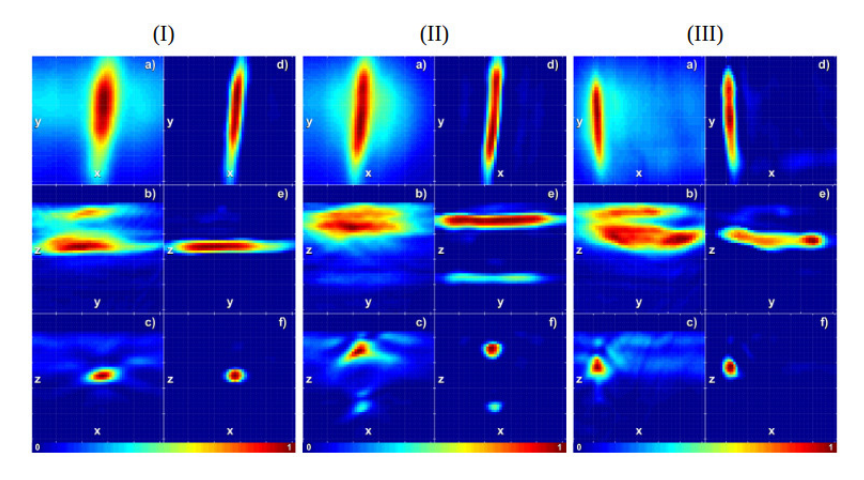


Fig. 8. Top- and side-view projections of the image prior to (left column) and after (right column) enhancement for each case studied in this article.

images (right column) of the experiments studied in this article (details are provided in Section IV). In the enhanced images, the main structures of the target of interest are highlighted while most of the background noise is removed.

Inspection of the enhanced image isosurfaces enables the choice of a threshold value that yields a 3-D solid model. Let η be the chosen threshold value by this image inspection. Define a classifier $\Delta_{\eta} : \mathbb{R}^3 \to [0, 1]$ as

$$\Delta_{\eta}(x) = \begin{cases} 0, & \text{if } x < \eta \\ 1, & \text{otherwise.} \end{cases}$$
 (13)

Then the 3-D model is obtained as the binarized image $\mathcal{M}_{3D}(P_j) = \Delta_{\eta}(\mathscr{E}(P_j)).$

B. Processing Pipeline

The multistatic GPR data-processing pipeline is summarized in Fig. 9. The input raw 3-D GPR data from each of three receivers are back-projected, normalized, and squared, and finally summed to compose a multistatic image. The resulting image is then enhanced using the JEF for 3-D modeling. A processing step that can be applied in the BPA image or as a preprocess in the GPR raw data is the removal of ground reflection. Performing mean subtraction is a common method to remove direct coupling and ground reflection but there is the risk of removing backscattered signals of targets that were parallel to the survey path. For underground utility applications, there is a minimum depth expected for pipelines, such that the image can be zeroed above that depth, or the BPA may be formed only in the region of interest, that is, define the domain of interest as a region starting an offset below the ground level.

IV. EXPERIMENTS

As shown in Fig. 10(a), a multistatic GPR system composed of a transmitter antenna and three receiver antennas was used to generate data sets in the laboratory experiments. The antennas are horn antennas whose operating band spans from 600 MHz to 6 GHz [27]. The system is controlled by a 4-channel Keysight PNA-X network analyzer to perform

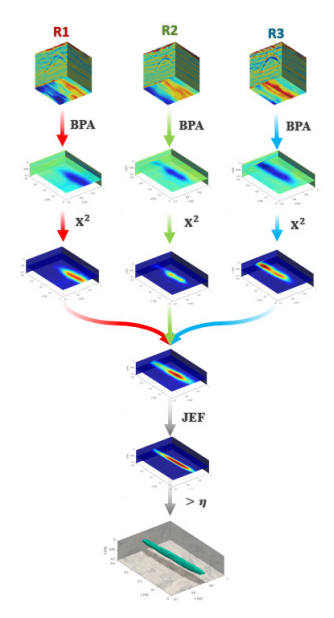


Fig. 9. GPR data-processing pipeline: raw GPR data for each receiver is given as input. The BPA is applied, and the resulting image squared and scaled. All receiver images are then summed. The multistatic image is enhanced using the JEF and binarized using a suitable threshold level.

frequency sweeping and scattering signal acquisition. The experiments are conducted on a sandbox where three test cases are implemented, each of which has a different object for detection. The first case is a 1 in (25.4 mm) polyvinyl chloride (PVC) pipe perpendicular to GPR scan direction shown in Fig. 11(I). The second case is a 4 in (116 mm) PVC pipe shown in Fig. 11(II). The third case is a U-shaped pipe of 2 in (50.8 mm) PVC pipe partially shown in Fig. 11(III). The dielectric constant ϵ of sand is 4. The pipes are buried at depths ranging from 1 in (25.4 mm) to 2 in (50.8 mm). For all cases, each B-scan image is composed of 80 A-scan traces taken approximately every 10-mm interval. Each B-scan is taken parallel and 1 in (25.4 mm) apart of each other, as illustrated in Fig. 10(b). In all cases, the pipes are hollow, that is, filled with air. This has an effect on the observed diameter, as will be pointed in case 2. The antenna radiation pattern is shown in Fig. 12.

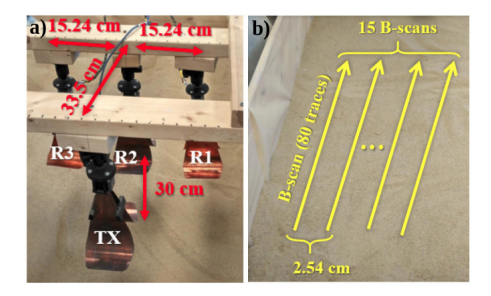


Fig. 10. Multistatic GPR antenna setup.

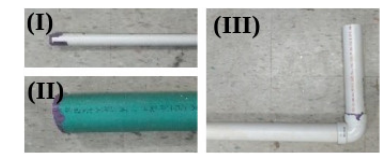


Fig. 11. Photograph of the 1 in PVC pipe.

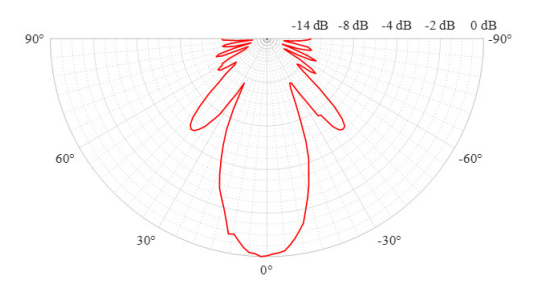


Fig. 12. Far-field horn antenna radiation pattern employed in the BPA.

The BPA images for cases 1 and 2 are computed in the region $[0.7, 1.0] \times [0, 0.4] \times [-0.1, 0]$ m³ discretized in $51 \times 51 \times 51$ points. For case 3, the BPA is computed in the region $[0.3, 0.9] \times [0, 0.4] \times [-0.1, 0]$ m³ and discretized in $61 \times 41 \times 51$ points. The cutoff threshold parameter of the JEF is set to $\tau = 1$. The filter scale was set to half the wavelength of the antenna's center frequency 3 GHz considering the wave speed on the ground, $\sigma \approx 25$ mm.

A. Case 1: 1 in PVC Pipe

Fig. 13(I) shows, from top-left to top-right, inserts of the first to third receiver for illustration purposes. Note the different regions of focus of each receive antenna. The main image shows the 3-D multistatic image prior to enhancement. Since the pipe diameter is at the order of magnitude of the emitted wavelengths, it is not possible to resolve the top and bottom surfaces. The resolved depth is about 2 in., which is in good agreement with the ground truth. Fig. 14(I) shows the enhanced image. Notice that the background noise level is greatly reduced. Finally, the 3-D model resulting from manually thresholding the image is shown in Fig. 15(I). Projections of the final model are shown in Fig. 16(I).

B. Case 2: 4" PVC Pipe

Fig. 13(II) shows, from top-left to top-right, inserts of the first to third receiver for illustration purposes. The main image shows the 3-D multistatic image. Good focusing is also achieved, especially of the top surface, shown in the slice. The diameter is large enough such that the top and the bottom of the pipe are identified. The resolved depth is

about 1 in., which is in good agreement with the ground truth. This is the pipe whose side-view is shown in Fig. 7. Notice that the distance between the top and bottom signal focus points shown in that image is about 50 mm, roughly half the expected diameter. This is because the pipe is filled with air, and the back-projection model assumes the entire subsurface region to have a dielectric constant of $\epsilon = 4$. This dielectric constant implies a wave speed of v = c/2, thus leading to half the expected diameter, since for the same flight time that speed covers half the distance that would be covered at the speed of light. Also, as both the top and bottom interfaces are resolved, it could lead to incorrect interpretation, for example, concluding that there are two buried targets. This is an uncertainty inherent in the raw GPR data, since two hyperbolas are formed. Some observations could be used to aid in distinguishing these two scenarios. For instance, it is rare that two distinct targets are perfectly aligned, whereas a single larger target will exhibit the alignment between the top and bottom interfaces. Also, as briefly discussed in Section II, signal polarity might inform the target material. If the top and bottom targets are of different materials, considering signal polarity might aid in distinguishing both cases. Fig. 14(II) shows the enhanced image. Notice that the background noise level is greatly reduced in this case as well. Finally, the 3-D model resulting from thresholding the image with a suitable value is shown in Fig. 15(II). The top- and side-view projections of the final model are presented in Fig. 16(II).

C. Case 3: 2 in U-Shaped PVC Pipe

Fig. 13(III) shows, from top-left to top-right, inserts of the first to third receiver for illustration purposes. The main image shows the 3-D multistatic image. Note the presence of a strong signal noise along the x-axis in the left insert. Furthermore, part of the pipe is aligned with the scan direction, preventing the application of traditional mean subtraction to raw GPR data. The inserts also indicate that the along-path section of the pipe is observed well by the third antenna (right insert) but poorly by the other antennas (left and center). A simple sum leads to a strong intensity on the section of the pipe perpendicular to the survey, which is observed by all antennas. The enhanced image, shown in Fig. 14(III), helps clearing the background noise and retains the information provided by the third antenna. The resolved depth is between 1 and 2 in., in agreement with the ground truth. The pipe joint region, however, is somewhat attenuated. Still, the enhanced image is superior for the purpose of generating the 3-D model. To extract a similar volume of the pipe as shown in Fig. 15(III) would generate a considerable noise region in the original 3-D image, especially due to the BPA bias present in the first antenna image. This is a challenging scenario since there is a presence of significant noise in one of the images, part of the target is observed only by few antennas, and the same target has regions of different intensity. A good 3-D model, shown in Fig. 15(III), is recovered albeit with some degree of ground noise. Top- and side-view projections of the final model are shown in Fig. 16(III).

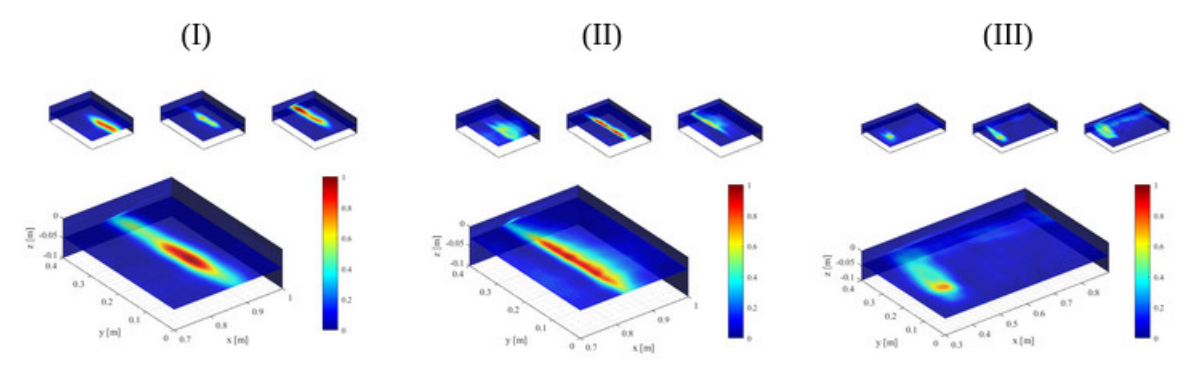


Fig. 13. Slice of the resulting multistatic image for each case. Inserts above illustrate, from left to right, receivers 1, 2, and 3 back-projected images.

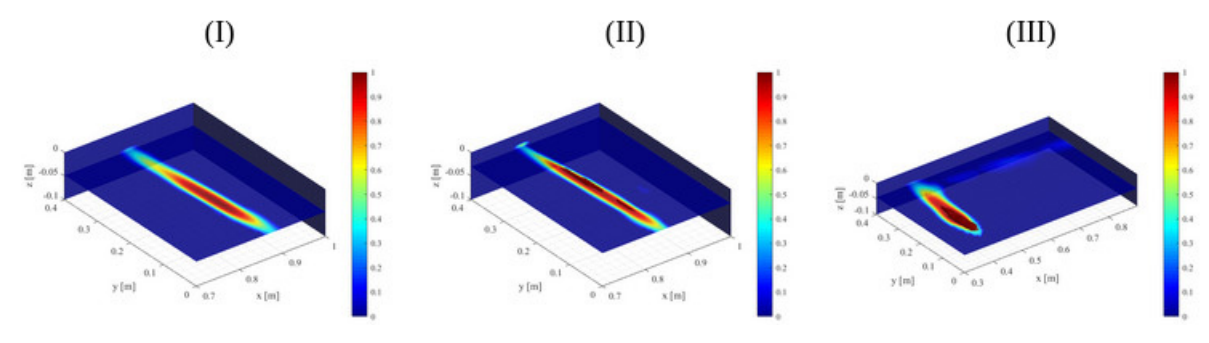


Fig. 14. Slice of the multistatic image enhanced by the Jerman filter for each case.

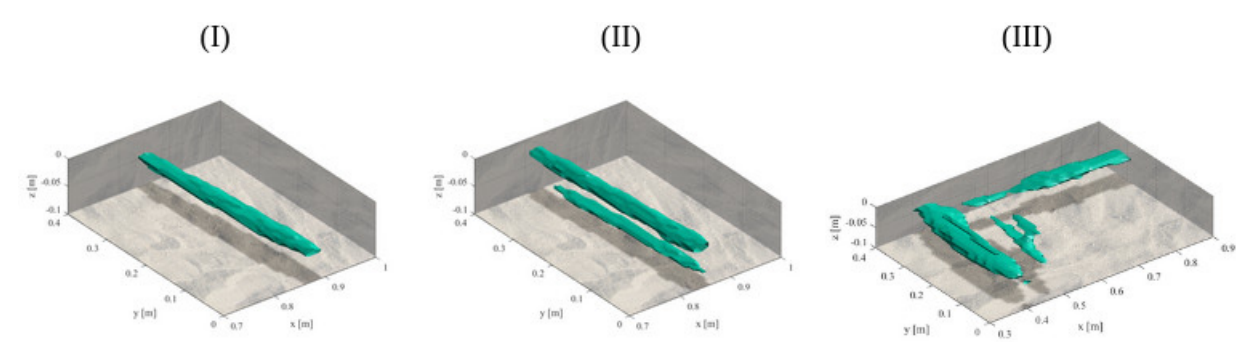


Fig. 15. Extracted solid after thresholding for each case.

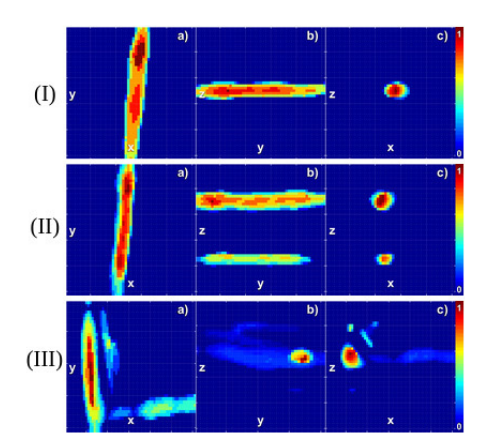


Fig. 16. Top- and side-view projections of the final model for each case.

V. CONCLUSION AND DISCUSSIONS

Most of the GPR imaging literature covers the 2-D, monolayer, monostatic case. The BPA applied here, based on [22], can be employed for 3-D bilayer multistatic GPR. In [22], two buried metallic objects of relatively simple shapes were

studied. Here, PVC pipes of different sizes and shapes are presented corroborating the good performance of the algorithm. Moreover, since the calculation of the wave travel times and addition to the final image may be performed with parallel computation, very short computation times can be achieved. For instance, for the largest images with over 130 000 image points, computation for each receiver image is performed under 5 s running in an Acer Predator Helios 300 PH315-51. It is possible to decrease computation time even further by leveraging on cloud cluster computing.

The JEF was very effective in enhancing the tubular structures imaged. To the author's knowledge, such filter technique has not been applied in GPR underground utilities survey before, nor in landmine or unexploded ordnance detection, which opens an invitation to investigate the transfer of knowledge from the medical imaging field to GPR applications and vice versa.

For the imaging GPR, the sensitivity is an important factor determining system's sensing performance. In this article, a sensitivity studied has not been performed, as in our laboratory settings, a sufficiently high SNR, between -10 and

−30 dB, was present. In the next step of research, the sensitivity effect in GPR field applications will be investigated. Some of the challenges in field applications are: higher signal loss, irregular interfaces, unknown dielectric constant, and so on. Furthermore, to be able to penetrate deeper into the ground, lower-frequency EM waves have to be employed. This will reduce the image resolution, potentially preventing the clear determination of the target shape, although the target position should still be recovered. Also, accurate position of the GPR system is required for correct back-projection. Most commercial GPR systems are equipped with either wheel encoders or GPS which typically present resolution on the meter range. Hence, there is a plethora of research opportunities on the path to field deployment. Those will be objects of our future research.

In conclusion, the application of a processing pipeline to GPR data, encompassing image reconstruction and enhancement, to create 3-D models of subsurface tubular structures toward advanced underground infrastructure visualization is demonstrated and validated.

REFERENCES

- H. M. Jol, Ground Penetrating Radar Theory and Applications, 1st ed. Amsterdam, The Netherlands: Elsevier, 2009.
- [2] J. D. Daniels, Ground Penetrating Radar, 2nd ed. London, U.K.: The Institution of Electrical Engineers, 2004.
- [3] Y. Zhang, D. Burns, D. Huston, and T. Xia, "Sand moisture assessment using instantaneous phase information in ground penetrating radar data," in *Proc. Struct. Health Monitor. Inspection Adv. Mater., Aerosp., Civil Infrastruct.*, vol. 9437, Apr. 2015, Art. no. 943726.
- [4] G. A. Mcmechan, G. C. Gaynor, and R. B. Szerbiak, "Use of ground-penetrating radar for 3-D sedimentological characterization of clastic reservoir analogs," *Geophysics*, vol. 62, no. 3, pp. 786–796, May 1997.
- [5] A. M. Alani, M. Aboutalebi, and G. Kilic, "Applications of ground penetrating radar (GPR) in bridge deck monitoring and assessment," *J. Appl. Geophys.*, vol. 97, pp. 45–54, Oct. 2013, doi: 10.1016/j. jappgeo.2013.04.009.
- [6] Z. W. Wang, M. Zhou, G. G. Slabaugh, J. Zhai, and T. Fang, "Automatic detection of bridge deck condition from ground penetrating radar images," *IEEE Trans. Autom. Sci. Eng.*, vol. 8, no. 3, pp. 633–640, Jul. 2011.
- [7] Y. Zhang, A. S. Venkatachalam, D. Huston, and T. Xia, "Advanced signal processing method for ground penetrating radar feature detection and enhancement," in *Proc. Nondestruct. Characterization Compos. Mater.*, *Aerosp. Eng., Civil Infrastruct., Homeland Secur.*, vol. 9063, Mar. 2014, Art. no. 906318.
- [8] M. Cornick, J. Koechling, B. Stanley, and B. Zhang, "Localizing ground penetrating RADAR: A step toward robust autonomous ground vehicle localization," *J. Field Robot.*, vol. 33, no. 1, pp. 82–102, Jan. 2016.
- [9] D. Huston, T. Xia, Y. Zhang, T. Fan, D. Orfeo, and J. Razinger, "Urban underground infrastructure mapping and assessment," in *Proc. Sensors* Smart Struct. Technol. Civil, Mech., Aerosp. Syst., Apr. 2017.
- [10] X. Xu, T. Xia, A. Venkatachalam, and D. Huston, "Development of high-speed ultrawideband ground-penetrating radar for rebar detection," *J. Eng. Mech.*, vol. 139, no. 3, pp. 272–285, Mar. 2013.
- [11] G. Schall et al., "Handheld Augmented Reality for underground infrastructure visualization," Pers. Ubiquitous Comput., vol. 13, no. 4, pp. 281–291, May 2009.
- [12] H.-L. Chi, S.-C. Kang, and X. Wang, "Research trends and opportunities of augmented reality applications in architecture, engineering, and construction," *Autom. Construct.*, vol. 33, pp. 116–122, Aug. 2013, doi: 10.1016/j.autcon.2012.12.017.
- [13] C. Özdemir, Ş. Demirci, E. Yiğit, and B. Yilmaz, "A review on migration methods in B-scan ground penetrating radar imaging," *Math. Problems Eng.*, vol. 2014, pp. 1–16, 2014.
- [14] R. H. Stolt, "Migration by fourier transform," *Geophysics*, vol. 43, no. 1, pp. 23–48, Feb. 1978.
- [15] W. A. Schneider, "Integral formulation for migration in two and three dimensions," *Geophysics*, vol. 43, no. 1, pp. 49–76, Feb. 1978.

- [16] M. Soumekh, Synthetic Aperture Radar Signal Processing With MATLAB Algorithms, 1st ed. New York, NY, USA: Wiley, 1999.
- [17] C. Gilmore, I. Jeffrey, and J. Lovetri, "Derivation and comparison of SAR and frequency-wavenumber migration within a common inverse scalar wave problem formulation," *IEEE Trans. Geosci. Remote Sens.*, vol. 44, no. 6, pp. 1454–1461, Jun. 2006.
- [18] C. Zhou et al., "Automatic multiscale enhancement and segmentation of pulmonary vessels in CT pulmonary angiography images for CAD applications," Med. Phys., vol. 34, no. 12, pp. 4567–4577, Nov. 2007.
- [19] A. F. Frangi, W. J. Niessen, K. L. Vincken, and M. A. Viergever, "Multiscale vessel enhancement filtering," in *Medical Image Computing and Computer-Assisted Intervention—MICCAI*, W. M. Wells, A. Colchester, and S. Delp, Eds. Berlin, Germany: Springer, 1998, pp. 130–137.
- [20] T. Jerman, F. Pernus, B. Likar, and Z. Spiclin, "Enhancement of vascular structures in 3D and 2D angiographic images," *IEEE Trans. Med. Imag.*, vol. 35, no. 9, pp. 2107–2118, Sep. 2016.
- [21] D. Lesage, E. D. Angelini, I. Bloch, and G. Funka-Lea, "A review of 3D vessel lumen segmentation techniques: Models, features and extraction schemes," *Med. Image Anal.*, vol. 13, no. 6, pp. 819–845, Dec. 2009, doi: 10.1016/j.media.2009.07.011.
- [22] M. Pereira, Y. Zhang, D. Orfeo, D. Burns, D. Huston, and T. Xia, "3D tomographic image reconstruction for multistatic ground penetrating radar," in *Proc. IEEE Radar Conf. (RadarConf)*, Apr. 2019.
- [23] L. Zhou, C. Huang, and Y. Su, "A fast back-projection algorithm based on cross correlation for GPR imaging," *IEEE Geosci. Remote Sens. Lett.*, vol. 9, no. 2, pp. 228–232, Mar. 2012.
- [24] Y. Sato et al., "Tissue classification based on 3D local intensity structures for volume rendering," *IEEE Trans. Visual. Comput. Graph.*, vol. 6, no. 2, pp. 160–180, Apr./Jun. 2000.
- [25] Q. Li, S. Sone, and K. Doi, "Selective enhancement filters for nodules, vessels, and airway walls in two- and three-dimensional CT scans," *Med. Phys.*, vol. 30, no. 8, pp. 2040–2051, Jul. 2003. [Online]. Available: https://aapm.onlinelibrary.wiley.com/doi/abs/10.1118/1.1581411
- [26] M. Erdt, M. Raspe, and M. Suehling, "Automatic hepatic vessel segmentation using graphics hardware," in *Medical Imaging and Augmented Reality*, T. Dohi, I. Sakuma, and H. Liao, Eds. Berlin, Germany: Springer, 2008, pp. 403–412.
- [27] A. Ahmed, Y. Zhang, D. Burns, D. Huston, and T. Xia, "Design of UWB antenna for air-coupled impulse ground-penetrating radar," *IEEE Geosci. Remote Sens. Lett.*, vol. 13, no. 1, pp. 92–96, Jan. 2016.



Mauricio Pereira received the B.Sc. degree in mechanical engineering from the University of Sao Paulo, Sao Carlos, Brazil, in 2016, and the M.Sc. degree in mechanical engineering from The University of Vermont, Burlington, VT, USA, in 2019. He is currently pursuing the Ph.D. degree in structural engineering with the Princeton University, Princeton, NJ, USA.

His research interests include signal processing, image formation, computer vision, augmented reality, structural health monitoring, and remote sensing.



Dylan Burns received the B.S. and M.S. degrees in mechanical engineering, with a minor in mathematics and the Ph.D. degree in mechanical engineering with his dissertation Ambulatory Lordosimeter Measurement and Feedback Control of Seated Posture from The University of Vermont, Burlington, VT, USA, in 2006 and 2011, respectively.

He is currently a Research Associate and a Lecturer with The University of Vermont.



Daniel Orfeo received the B.S. degree in mathematics, with a minor in physics, and the M.S. degree in mechanical engineering from The University of Vermont (UVM), Burlington, VT, USA, in 2014 and 2018, respectively, where he is currently pursuing the Ph.D. degree in mechanical engineering.

His research interests include microwave and magnetic sensing and communications.



Yu Zhang received the B.S. degree in electrical engineering from the Huazhong University of Science and Technology, Wuhan, China, in 2012, and the Ph.D. degree in electrical engineering from The University of Vermont, Burlington, VT, USA, in 2017.

In 2017, he joined Aptiv PLC, Agoura Hills, CA, USA, where he is currently a Senior Radar System Engineer working on automotive radar. His research interests include radar systems design and signal processing.



Dryver Huston received the B.S. degree from the University of Pennsylvania, Philadelphia, PA, USA, and the M.A. and Ph.D. degrees from Princeton University, Princeton, NJ, USA, in 1983 and 1986, respectively.

Since 1987, he has been a Faculty Member with The University of Vermont, Burlington, VT, USA. He has authored the book, *Structural Sensing, Health Monitoring, and Performance Evaluation*.



Liangbao Jiao received the Ph.D. degree from Nanjing University, Nanjing, China, in 2006.

He is currently a Professor with the Institute of Industrial Technology, Nanjing Institute of Technology, Nanjing, China. His research interests focus on video and image process and artificial intelligence.



Tian Xia (Senior Member, IEEE) received the B.E. degree in electrical engineering from the Huazhong University of Science and Technology, Wuhan, China, in 1994, the M.S. degree from the Nanjing University of Posts and Telecommunications, Nanjing, China, in 2000, and the Ph.D. degree in electrical and computer engineering from The University of Rhode Island, Kingston, RI, USA, in 2003.

He is currently a Professor with the Department of Electrical Engineering, The University of Vermont, Burlington, VT, USA. His research interests focus

on sensor circuit design and signal processing.